aerospace

MDPI

Article

Bearing-Only Three-UAV Cooperative Target Localization with Adaptive Weighting and Configuration Optimization

Kangkang Li [1], Haodong Sun [1], Chao Cheng [2], Zhongjing Ren [2,3,4], Jianping Yuan [1,5] and Mengbi Wang [2,6,7,*]

[1] Weiqiao-UCAS (Binzhou) Science and Technology Co., Ltd., Binzhou 256600, China; li_214_kang_kang@163.com (K.L.); veastsun2023@gmail.com (H.S.); jyuan@nwpu.edu.cn (J.Y.)
[2] Binzhou Institute of Technology, Binzhou 256600, China; c.cheng@bjtu.edu.cn (C.C.); zren@sdu.edu.cn (Z.R.)
[3] School of Mechanical Engineering, Shandong University, Jinan 250061, China
[4] Shenzhen Research Institute of Shandong University, Shenzhen 518057, China
[5] School of Astronautics, Northwestern Polytechnical University, Xi'an 710072, China
[6] Department of Precision Instrument, Tsinghua University, Beijing 100084, China
[7] Weiqiao-UCAS (Beijing) Science and Technology Co., Ltd., Beijing 100083, China
* Correspondence: tortoise_wang@foxmail.com

Abstract

This paper addresses bearing-only three-dimensional target localization using three cooperative UAVs under observation inconsistency and degraded geometry. A weighted point-to-line least-squares localization model is established to fuse multiple line-of-sight (LOS) observations derived from image measurements, camera calibration, and UAV poses. To handle unreliable measurements without ground truth, a reliability assessment mechanism is developed by combining geometric stability indicators with observation consistency metrics, enabling weak geometry and abnormal observations to be identified online. Based on this assessment, an adaptive optimization framework is introduced to perform residual-driven adaptive weighting and configuration optimization, thereby suppressing unreliable LOS measurements and improving the conditioning of cooperative geometry. Simulation results under four representative scenarios show that the proposed method consistently improves localization accuracy and robustness. The mean localization error is reduced from 0.545 m to 0.260 m under abnormal observations, from 0.355 m to 0.081 m under degraded geometry, and from 0.711 m to 0.280 m when both effects occur simultaneously. Statistical evaluations including RMSE, standard deviation, maximum error, confidence intervals, and box-plot analysis further demonstrate that the proposed framework effectively reduces error dispersion and improves robustness.

Keywords: bearing-only localization; cooperative target localization; line-of-sight observation; reliability assessment; adaptive weighting; configuration optimization

Check for updates

Academic Editor: Gokhan Inalhan

Received: 27 May 2026
Revised: 20 June 2026
Accepted: 22 June 2026
Published: 22 June 2026

Copyright: © 2026 by the authors. Licensee MDPI, Basel, Switzerland. This article is an open access article distributed under the terms and conditions of the Creative Commons Attribution (CC BY) license.

1. Introduction

In recent years, unmanned aerial vehicles (UAVs) have been widely applied in civilian domains such as agriculture [1], transportation [2], inspection [3], and rescue [4], as well as in military tasks including reconnaissance [5] and strike [6], owing to their low cost and high maneuverability [7]. Target localization is a fundamental capability in UAV systems and plays an important role in visual navigation, scene monitoring, and precision guidance. Among existing sensing modalities, bearing-only localization [8] has attracted considerable attention because vision sensors are compact, lightweight, and power-efficient [9–12].

Despite these advantages, bearing-only localization remains challenging. For a single UAV, an image measurement provides only a line-of-sight (LOS) direction, while the target range is not directly observable. As a result, accurate three-dimensional localization usually relies on platform motion over time, which is sensitive to maneuver quality and measurement noise [13–15]. Multi-UAV cooperative localization alleviates this limitation by introducing simultaneous multi-view observations, thereby improving spatial constraints and estimation accuracy [16–20]. Representative studies have explored filtering-based fusion [21], direct LOS intersection via residual minimization [22], and formation adjustment through coordinated UAV motion [23].

However, several issues remain insufficiently addressed. First, many existing methods treat visual measurements as noisy state observations without fully considering the uncertainty propagation through the entire sensing pipeline, including pixel detection, camera calibration, and pose transformation [24–29]. Second, the numerical stability of multi-LOS intersection depends strongly on the geometric configuration of the observing UAVs; unfavorable geometries can greatly amplify small observation errors [30–34]. Third, ground-truth target positions are usually unavailable online, making it difficult to assess whether the current estimate is reliable and what corrective action should be taken. The challenge, therefore, is not only to compute a target position estimate, but also to assess its trustworthiness and adapt the cooperative strategy accordingly.

Although recent multi-UAV bearing-only studies have reported encouraging progress, many of them mainly focus on multi-frame target tracking, distributed filtering, or tracking–control integration. In contrast, this paper addresses frame-wise cooperative localization under unreliable visual observations and weak geometric configurations. The emphasis is placed on reliability-aware localization, adaptive observation handling, and geometry-aware formation adjustment within a unified framework. Specifically, a three-UAV cooperative localization model is established by explicitly mapping image-plane measurements, camera parameters, and UAV poses to LOS observations. The target position is then estimated through weighted point-to-line least squares. On this basis, localization reliability is evaluated online by combining geometric stability indicators with observation consistency metrics, without requiring ground truth. According to the estimated reliability, adaptive weighting and configuration optimization are triggered to suppress abnormal observations and improve the conditioning of LOS intersection.

The main contributions of this paper are summarized as follows:

- A weighted three-UAV bearing-only localization model is established using point-to-line least squares, which provides a unified geometric fusion framework for multiple LOS observations.
- A ground-truth-free reliability assessment mechanism is developed by combining geometric stability indicators and observation consistency metrics, enabling online distinction between weak geometry and abnormal observations.
- An adaptive optimization framework integrating residual-driven adaptive weighting and configuration optimization is proposed to improve robustness against unreliable observations and enhance localization performance under degraded geometric conditions.

The remainder of this paper is organized as follows. Section 2 presents the three-UAV cooperative localization model. Section 3 introduces the proposed reliability assessment method, including geometric stability analysis and observation consistency evaluation. Section 4 describes the adaptive optimization framework with adaptive weighting and configuration optimization. Section 5 reports the simulation results. Section 6 provides further discussion of the method, including its computational characteristics, applicability, and limitations. Section 7 concludes the paper.

2. Bearing-Only Three-UAV Cooperative Localization Model

2.1. Rationale for Three-UAV Cooperative Localization

Under ideal noise-free conditions, the three-dimensional position of a target can in principle be determined from two bearing observations. Geometrically, each bearing measurement defines a line-of-sight (LOS) ray, and the target position is obtained from the intersection of the two rays. Therefore, two UAVs provide the minimum number of observations required for a unique solution in the ideal case.

However, practical visual localization differs significantly from this idealized situation. Bearing measurements are inevitably affected by pixel noise, partial occlusion, false detections, attitude uncertainty, and calibration errors. Consequently, the LOS rays generally do not intersect at a single point. The localization problem must then be solved in a least-squares sense, and the solution becomes highly sensitive to small angular perturbations, particularly when the LOS rays are nearly parallel or intersect at a small angle.

From an estimation perspective, each LOS observation provides two independent angular constraints, while the target position contains three unknown coordinates. Two UAVs therefore provide exactly four scalar constraints for three unknowns, leaving no measurement redundancy for reliability evaluation or error suppression. In contrast, introducing a third UAV adds an additional independent LOS observation and creates an overdetermined localization system. The resulting redundancy enables observation consistency assessment, residual analysis, and robustness enhancement through adaptive weighting.

Furthermore, the additional LOS observation improves geometric conditioning. With only two UAVs, localization accuracy strongly depends on the intersection angle between the two LOS rays, and depth estimation may become highly unstable under unfavorable configurations. The third LOS observation provides an independent geometric constraint that helps reduce error amplification and improves observability in weak-geometry conditions.

For these reasons, three UAVs can be regarded as the minimum robust structure for bearing-only cooperative localization. While two UAVs are theoretically sufficient for localization under ideal conditions, three UAVs constitute the smallest configuration that simultaneously provides localization capability, measurement redundancy, observation-consistency verification, and geometric robustness.

Moreover, a larger multi-UAV localization system can be viewed as an extension of multiple three-UAV cooperative units. Core issues such as LOS observation modeling, geometric conditioning, error amplification, and observation inconsistency are already reflected in the three-UAV case. Once these mechanisms are properly formulated in the minimal robust setting, they can be extended to larger systems with additional considerations such as communication, synchronization, and distributed computation. For this reason, this paper focuses on the three-UAV cooperative localization problem.

2.2. LOS Observation Model and Geometric Residual

At time frame t, the i-th UAV detects the target at image coordinates $(u_i(t), v_i(t))$. Using the camera intrinsic matrix $\mathbf{K}$, the normalized LOS direction in the camera coordinate system is expressed as

$$\mathbf{d}_i^c(t) = \frac{\mathbf{K}^{-1}[u_i(t), v_i(t), 1]^{\mathrm{T}}}{\|\mathbf{K}^{-1}[u_i(t), v_i(t), 1]^{\mathrm{T}}\|}. \tag{1}$$

By further incorporating the camera-to-body rotation matrix $\mathbf{R}_{c\to b}$ and the UAV attitude matrix $\mathbf{R}_i(t)$, the LOS direction in the world coordinate system is obtained as

$$\mathbf{d}_i(t) = \mathbf{R}_i(t)\mathbf{R}_{c\to b}\mathbf{d}_i^c(t), \quad \|\mathbf{d}_i(t)\| = 1. \tag{2}$$

This unit vector describes the spatial viewing direction from the UAV toward the target and serves as the basic observation used for cooperative localization.

In practical systems, the LOS direction may also be affected by EO/IR gimbal attitude errors, camera mounting errors, and UAV attitude estimation errors. These factors introduce angular perturbations into the transformed LOS vector and can therefore be modeled as uncertainties associated with $\mathbf{d}_i(t)$. Since the objective of this paper is to improve localization robustness under unreliable LOS observations rather than to calibrate individual sensor error sources, such effects are treated as perturbations of the LOS direction in the simulation framework.

Let the position of the i-th UAV at time t be $\mathbf{p}_i(t)$, and let its corresponding LOS direction be $\mathbf{d}_i(t)$. For any candidate target position $\mathbf{p}_{obj}(t)$, the orthogonal geometric residual with respect to the i-th LOS is defined as

$$\mathbf{e}_i(t) = \Big(\mathbf{I} - \mathbf{d}_i(t)\mathbf{d}_i^{\mathrm{T}}(t)\Big)\Big(\mathbf{p}_{obj}(t) - \mathbf{p}_i(t)\Big), \tag{3}$$

where $\mathbf{I}$ is the identity matrix.

The residual vector represents the shortest displacement from the candidate target position to the corresponding LOS. In the ideal case, all residuals are zero, meaning that the estimated target position lies exactly on all LOS rays. In practice, nonzero residuals reflect the geometric inconsistency introduced by observation noise and modeling errors.

2.3. Weighted Point-to-Line Least-Squares Localization

Because noisy LOS observations generally do not intersect at a single point, the target position is estimated by minimizing the weighted sum of point-to-line distances over all LOS observations:

$$\min_{\mathbf{p}_{obj}(t)} \sum_{i=1}^{3} w_i \|\mathbf{e}_i(t)\|^2, \tag{4}$$

where w_i denotes the weight of the i-th observation. Assuming independent Gaussian measurement errors, the weighted least-squares formulation corresponds to the maximum-likelihood estimator. Therefore, the optimal weighting coefficient is inversely proportional to the measurement variance,

$$w_i \propto \frac{1}{\sigma_i^2}, \tag{5}$$

where σ_i^2 denotes the uncertainty of the corresponding LOS observation.

In practical vision-based UAV localization systems, the LOS uncertainty is mainly affected by image measurement noise and target detection reliability. Therefore, the initial weight is defined as

$$w_i = \frac{c_i}{\sigma_{px,i}^2}, \tag{6}$$

where c_i is the detection confidence provided by the perception module and $\sigma_{px,i}$ is the pixel noise standard deviation of the corresponding camera. Consequently, observations with higher confidence and lower measurement uncertainty contribute more to the localization solution. The detailed noise propagation analysis and parameter interpretation are further discussed in Section 4.4.

The weight reflects the reliability of the corresponding LOS measurement and can be designed according to factors such as detection confidence, propagated pixel uncertainty, or adaptive reliability adjustment.

The geometric interpretation of the three-UAV cooperative localization model is illustrated in Figure 1.

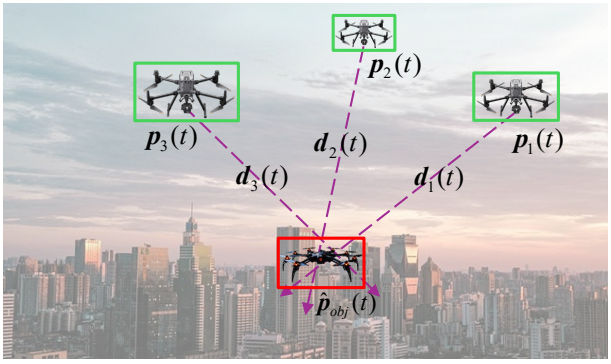


Figure 1. Schematic diagram of bearing-only three-UAV cooperative target localization. Green boxes denote the localization UAVs, red box denotes the observed target, and arrows indicate the line-of-sight (LOS) directions.

The above optimization problem is quadratic with respect to $\mathbf{p}_{obj}(t)$ and admits a closed-form least-squares solution. By setting the first-order derivative to zero, the localization problem can be written as

$$\mathbf{A}(t)\mathbf{p}_{obj}(t) = \mathbf{b}(t), \tag{7}$$

where

$$\mathbf{A}(t) = \sum_{i=1}^{3} w_i \left(\mathbf{I} - \mathbf{d}_i(t)\mathbf{d}_i^{\mathrm{T}}(t)\right), \tag{8}$$

$$\mathbf{b}(t) = \sum_{i=1}^{3} w_i \left(\mathbf{I} - \mathbf{d}_i(t)\mathbf{d}_i^{\mathrm{T}}(t)\right)\mathbf{p}_i(t). \tag{9}$$

When $\mathbf{A}(t)$ is full rank, the unique localization solution is

$$\mathbf{p}_{obj}(t) = \mathbf{A}^{-1}(t)\mathbf{b}(t). \tag{10}$$

When $\mathbf{A}(t)$ is ill-conditioned or singular, the Moore–Penrose pseudoinverse can be used instead:

$$\mathbf{p}_{obj}(t) = \mathbf{A}^{\dagger}(t)\mathbf{b}(t). \tag{11}$$

Therefore, the proposed model provides a compact and computationally efficient geometric fusion framework for bearing-only cooperative localization, which also serves as the basis for the subsequent reliability assessment and adaptive optimization.

3. Reliability Assessment for Three-UAV Cooperative Localization

The previous section established a weighted three-UAV cooperative localization model based on bearing-only measurements, where the target position is estimated as the point that best satisfies the geometric consistency of three LOS vectors. The localization error depends on both LOS measurement noise and geometric configuration. Since ground-truth target positions are unavailable in practical systems, the localization error cannot be directly computed. Therefore, it is necessary to develop a ground-truth-free, online reliability assessment mechanism to evaluate the quality of the current estimate and to support subsequent adaptive weighting and configuration optimization.

3.1. Geometric Stability Characterization

Measurement uncertainties arising from pixel detection errors, attitude estimation inaccuracies, and extrinsic calibration biases ultimately manifest as perturbations in LOS direction vectors. The measured LOS direction of the i-th UAV can be expressed as

$$\mathbf{d}_i(t) = \mathbf{d}_i^*(t) + \delta\mathbf{d}_i(t), \tag{12}$$

where $\mathbf{d}_i^*(t)$ is the ideal direction and $\delta\mathbf{d}_i(t)$ is a small perturbation.

Substituting this into the normal equations and applying first-order approximation reveals that the position estimation error exhibits a typical inverse-matrix amplification structure, where direction errors are mapped and amplified through $\mathbf{A}^{-1}(t)$.

The matrix $\mathbf{A}(t)$ characterizes the joint constraint strength imposed by the three LOS vectors, while $\mathbf{A}^{-1}(t)$ reflects the sensitivity of the solution to observation perturbations. When the configuration weakens constraints along certain directions, $\mathbf{A}(t)$ becomes ill-conditioned, causing large gains in $\mathbf{A}^{-1}(t)$ and significant error amplification.

Thus, geometric stability can be characterized online by analyzing the spectral properties of $\mathbf{A}(t)$. Since $\mathbf{A}(t)$ is symmetric, its eigen-decomposition is

$$\mathbf{A}(t) = \mathbf{V}(t)\mathbf{\Lambda}(t)\mathbf{V}^{\mathrm{T}}(t), \tag{13}$$

where

$$\mathbf{\Lambda}(t) = \mathrm{diag}(\lambda_1(t), \lambda_2(t), \lambda_3(t)), \quad \lambda_1(t) > \lambda_2(t) > \lambda_3(t), \tag{14}$$

and $\mathbf{V}(t) = [\mathbf{v}_1(t), \mathbf{v}_2(t), \mathbf{v}_3(t)]$ contains the corresponding eigenvectors.

This decomposition reflects the anisotropy of geometric constraints. Larger eigenvalues indicate stronger constraints and lower sensitivity to noise along the corresponding directions. The smallest eigenvalue $\lambda_3(t)$ represents the weakest constraint direction, and its eigenvector $\mathbf{v}_3(t)$ indicates the direction in which errors are most likely to be amplified. Even when the system is nominally solvable, a small $\lambda_3(t)$ can lead to severe instability.

Based on this, several complementary metrics are defined to quantify geometric stability from four perspectives.

1. Overall uncertainty metric:

$$\mathcal{T}(t) = \sum_{k=1}^{3} \frac{1}{\lambda_k(t)}, \tag{15}$$

   which approximates the total variance of the position estimate under comparable noise levels. Larger values indicate higher sensitivity and lower stability.

2. Weakest constraint strength and sensitive direction:

$$\lambda_3(t), \quad \mathbf{v}_3(t), \tag{16}$$

   which directly characterize the weakest constrained direction and provide actionable information for configuration optimization.

3. Anisotropy metric:

$$\kappa(t) = \frac{\lambda_1(t)}{\lambda_3(t)}, \tag{17}$$

   which measures the imbalance of constraints across directions. Larger values indicate stronger anisotropy and higher sensitivity to perturbations, typically associated with near-degenerate configurations.

4. Overall geometric constraint strength:

$$\mathcal{D}(t) = \prod_{k=1}^{3} \lambda_k(t), \tag{18}$$

which provides a global measure of constraint strength. Larger values generally correspond to stronger multi-view constraints and lower overall uncertainty, making it suitable for configuration comparison and optimization.

3.2. Observation Consistency Evaluation

The previous subsection characterized geometric stability via the spectral properties of $\mathbf{A}(t)$, reflecting the intrinsic sensitivity of the solution under a given configuration and weighting scheme. However, strong geometric constraints do not guarantee correctness. In real visual pipelines, factors such as false detections, occlusions, bounding box jitter, and pose estimation errors may cause one UAV's LOS measurement to be inconsistent with others, leading to biased estimates driven by outliers.

Therefore, an additional observation consistency evaluation is required based on the geometric self-consistency between the solution and observations.

Given the estimated target position $\mathbf{p}_{obj}(t)$ at time t, the residual norm for the i-th LOS is

$$r_i(t) = \|\mathbf{e}_i(t)\|, \tag{19}$$

and the weighted residual energy is defined as

$$J(t) = \sum_{i=1}^{3} w_i r_i^2(t). \tag{20}$$

Here, $r_i(t)$ measures the geometric deviation between the solution and the i-th LOS, while $J(t)$ reflects the overall consistency of all observations. When observations are consistent, $\mathbf{p}_{obj}(t)$ lies close to all LOSs, resulting in a small $J(t)$. In contrast, outliers typically cause a significant increase in $J(t)$, often accompanied by a large individual residual.

For practical threshold design and experimental evaluation, the residual can be further normalized by its propagated standard deviation:

$$\rho_i(t) = \frac{r_i(t)}{\sigma_{r,i}(t)}, \tag{21}$$

where $\sigma_{r,i}(t)$ denotes the propagated residual uncertainty of the i-th LOS observation. The normalized residual $\rho_i(t)$ measures the deviation of the current LOS residual relative to its expected noise scale. Accordingly, the largest normalized residual is defined as

$$\rho_{\max}(t) = \max_i \rho_i(t). \tag{22}$$

Under the special choice $w_i = 1/\sigma_{r,i}^2(t)$, the weighted residual energy $J(t)$ becomes the normalized consistency metric used in the simulations. Thus, the experimental implementation does not introduce a different metric, but adopts a normalized realization of the same consistency measure. The detailed relationship between these quantities and the corresponding threshold design is discussed in Section 4.4.

Based on these residuals, a two-level evaluation strategy is adopted.

1. Global consistency metric: $J(t)$

If $J(t)$ exceeds a threshold, the current frame is considered geometrically inconsistent, indicating potential outliers. In the experimental evaluation, this criterion is implemented through its normalized form.

2. Individual outlier indicator: $\rho_{\max}(t)$
   A significantly large normalized residual indicates that at least one LOS observation is inconsistent with the current estimate beyond its nominal uncertainty range.

Two important remarks are noted:

- The observation consistency metrics do not directly estimate true localization error, but instead assess the self-consistency between observations and the solution. Poor consistency indicates that the estimate may be dominated by outliers and should not be directly used for decision-making, even if geometric metrics appear favorable. Conversely, good consistency implies that the estimate likely lies near the true intersection, with its accuracy mainly governed by geometric strength and noise levels.
- Observation consistency and geometric stability capture different aspects: the former evaluates measurement self-consistency, while the latter reflects constraint strength. Their combination enables better diagnosis of error sources. Specifically, if $\mathbf{A}(t)$ is ill-conditioned but the consistency metric remains small, the issue is likely weak geometry, suggesting configuration optimization. If the consistency metric becomes large while $\mathbf{A}(t)$ remains well-conditioned, the issue is more likely to be observation inconsistency, requiring measurement-level handling such as adaptive weighting or temporary rejection of the current estimate.

3.3. Reliability States and Triggering Mechanism

The previous subsections established computable indicators for localization quality from both geometric and observation perspectives. In the absence of ground truth, a single metric is insufficient to cover all failure modes: weak geometric constraints may lead to high sensitivity to noise, while outlier observations may bias the solution even under favorable geometry. Therefore, this subsection fuses both types of evidence to construct a reliability assessment and triggering mechanism, providing a unified and interpretable decision input for subsequent adaptive adjustment.

3.3.1. State Definition

Based on the geometric metrics in Section 3.1 and the observation consistency metrics in Section 3.2, the localization quality at the current frame is classified into three states:

- S0 (Reliable): Geometrically stable and observation-consistent; the solution can be directly used for downstream tasks;
- S1 (Weak Geometry): Observations are consistent, but geometric constraints are insufficient; the solution is sensitive to noise and requires configuration enhancement;
- S2 (Observation-Inconsistent): Observations are inconsistent, indicating potential outliers; observation-level processing (e.g., down-weighting, rejection, or re-estimation) is required, or the current solution should be temporarily discarded.

This three-state classification aims to distinguish between geometric deficiencies and observation anomalies without relying on ground truth, thereby providing interpretable triggers and task allocation for subsequent adaptive strategies.

3.3.2. Threshold-Based Decision Rules and Trigger Conditions

To enable real-time and reproducible reliability assessment, threshold-based rules are applied to geometric stability and observation consistency. Specifically, the geometric stability condition is defined as

$$\lambda_3(t) > \tau_\lambda, \quad \kappa(t) < \tau_\kappa, \tag{23}$$

and the observation consistency condition is defined as

$$J(t) < \tau_J, \quad \rho_{\max}(t) < \tau_\rho, \tag{24}$$

where τ_λ, τ_κ, τ_J, and τ_ρ denote the corresponding threshold parameters, whose determination and normalized implementation are discussed in Section 4.4. Geometric indicators $(\lambda_3(t), \kappa(t))$ detect weak constraints and degeneracy, preventing numerical instability under near-degenerate configurations. Observation consistency metrics $(J(t), \rho_{\max}(t))$ identify global inconsistency and individual outliers, avoiding biased solutions caused by erroneous LOS measurements.

Based on these conditions, the reliability assessment and triggering rules are established, as shown in Figure 2.

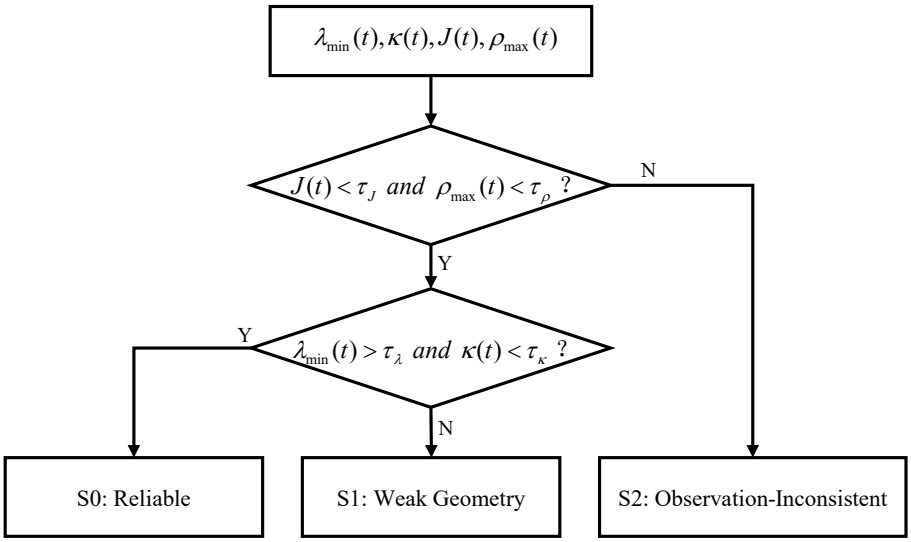


Figure 2. Flowchart for determining localization reliability states.

- If both geometric stability and observation consistency conditions are satisfied, the state is classified as S0 (Reliable).
- If observation consistency is satisfied but geometric stability is violated (e.g., small $\lambda_3(t)$ or large $\kappa(t)$), the state is classified as S1 (Weak Geometry).
- If observation consistency is violated, the state is classified as S2 (Observation-Inconsistent). In this case, the issue is attributed to the observation side, and observation quality must be handled before configuration optimization is considered.

When observation inconsistency occurs, directly using the current estimate or adjusting configuration based on it may lead to incorrect decisions; thus, outliers should first be identified and suppressed. Conversely, when observations are consistent but geometry is weak, the primary risk arises from error amplification, and configuration enhancement is more appropriate.

This subsection establishes a reliability assessment and triggering mechanism based on both geometric and observation metrics under ground-truth-free conditions. The geo-

metric indicators $(\lambda_3(t), \kappa(t))$ characterize numerical stability and degeneracy risk, while the observation consistency metrics detect outliers and inconsistencies. Together, they determine whether the current estimate should be accepted and which corrective action should be triggered.

In addition, the overall geometric strength and uncertainty metrics introduced in Section 3.1 quantify configuration quality from complementary perspectives and are suitable as objective functions for subsequent optimization. Based on the proposed reliability assessment, the next section develops adaptive weighting and configuration optimization methods to suppress outliers and actively improve cooperative geometry, thereby enhancing localization accuracy and robustness.

4. Adaptive Optimization Based on Reliability Assessment

Although the weighted three-UAV localization model established in Section 2 provides an efficient bearing-only localization solution under given observations and configurations, two typical degradation modes may arise in practice: observation inconsistency, where abnormal LOS measurements bias the estimate, and weak geometry, where insufficient directional constraints amplify localization errors. To improve reliability and robustness, this section develops an online adaptive optimization framework that combines adaptive weighting and configuration optimization under the guidance of the reliability assessment introduced in Section 3.

4.1. Overall Framework

The proposed framework takes the weighted localization model in Section 2 as the core estimator and uses the geometric and observation metrics from Section 3 as feedback signals. At each update cycle, a closed-loop process of estimation, evaluation, adaptation, and re-estimation is executed.

- Inputs: synchronized LOS observations $\{\mathbf{p}_i(t), \mathbf{d}_i(t), w_i(t)\}_{i=1}^{3}$;
- Outputs: updated observation weights $w_i(t+1)$ and configuration adjustment commands $\mathbf{p}_i^{\mathrm{cmd}}(t)$.

The overall procedure is summarized as follows and illustrated in Figure 3.

1. Observation synchronization and LOS construction: each UAV computes its current position $\mathbf{p}_i(t)$ and LOS direction $\mathbf{d}_i(t)$, and sends them to the cooperative estimation module.
2. Weighted localization: the target position is estimated using the weighted point-to-line least-squares model in Section 2, with the pseudoinverse adopted when the localization matrix is ill-conditioned.
3. Reliability evaluation: the geometric metrics $(\lambda_3(t), \kappa(t))$ and the observation consistency metrics $(J(t), \rho_{\max}(t))$ are computed.
4. State classification and strategy selection:
   - if observation inconsistency is detected, adaptive weighting is triggered;
   - if the observations are consistent but the geometry is weak, configuration optimization is triggered;
   - otherwise, the current estimate and configuration are maintained.
5. Adaptive weighting: the observation weights are updated to suppress unreliable LOS measurements, followed by re-estimation and consistency re-evaluation.
6. Configuration optimization: if weak geometry is detected under consistent observations, UAV adjustment commands are generated to improve cooperative geometry.
7. Closed-loop update: the updated weights and configuration commands are output, and the system proceeds to the next cycle.

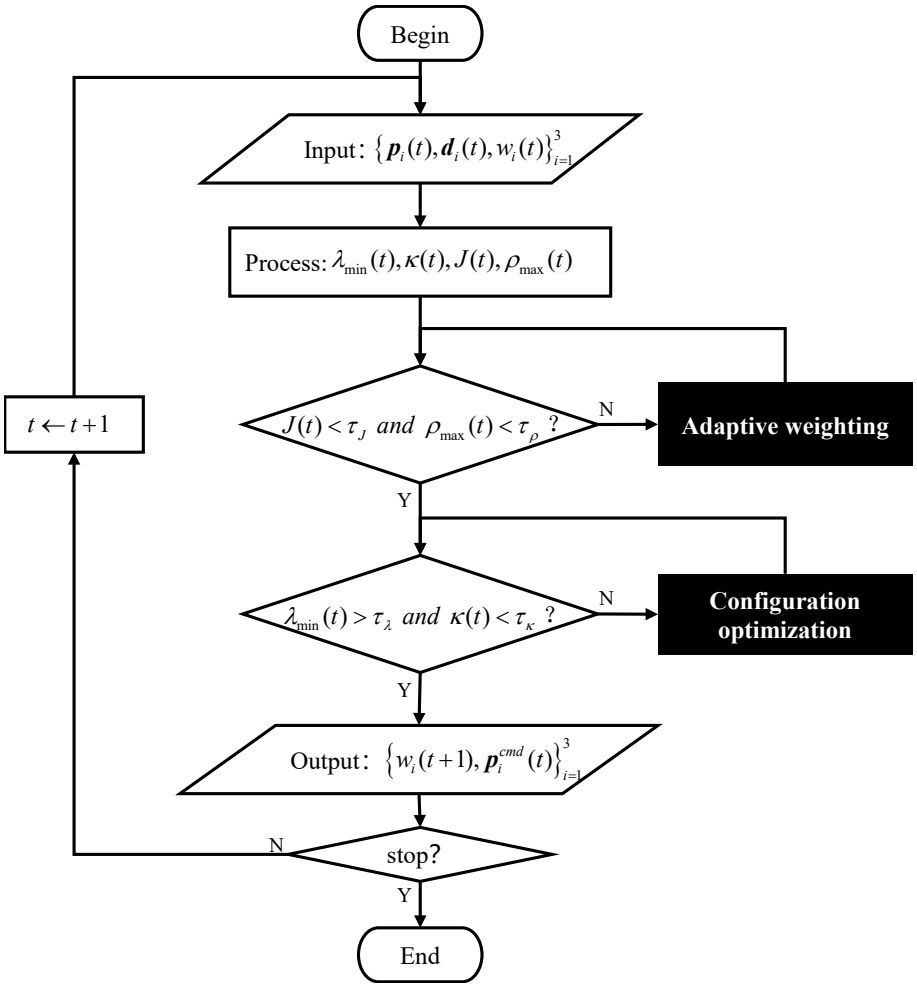


Figure 3. Flowchart of the adaptive optimization framework based on reliability assessment.

4.2. Adaptive Weighting

Adaptive weighting is introduced to suppress the influence of abnormal LOS observations when the current frame is classified as observation-inconsistent. In this case, observation-level correction is prioritized over configuration adjustment, because geometry optimization based on biased observations may lead to incorrect motion commands.

For the i-th LOS, let $\sigma_{r,i}(t)$ denote the propagated residual standard deviation. The corresponding normalized residual is defined as

$$x_i(t) = \frac{r_i(t)}{\sigma_{r,i}(t)}. \tag{25}$$

A Cauchy-type robust weighting function is then adopted:

$$\psi(x) = \frac{1}{1+x^2}. \tag{26}$$

Accordingly, the updated weight is written as

$$\tilde{w}_i(t+1) = w_i(t)\,\psi(x_i(t)). \tag{27}$$

To avoid permanent exclusion of any observation, a lower bound is imposed:

$$\bar{w}_i(t+1) = \max\left(\tilde{w}_i(t+1),\, w_{\min}\right). \tag{28}$$

The weights are then normalized:

$$w_i(t+1) = \frac{\bar{w}_i(t+1)}{\sum_{j=1}^{3} \bar{w}_j(t+1)}. \tag{29}$$

After the weight update, the target position is re-estimated using

$$\hat{\mathbf{A}}(t) = \sum_{i=1}^{3} w_i(t+1)\left(\mathbf{I} - \mathbf{d}_i(t)\mathbf{d}_i^{\mathrm{T}}(t)\right), \tag{30}$$

$$\hat{\mathbf{b}}(t) = \sum_{i=1}^{3} w_i(t+1)\left(\mathbf{I} - \mathbf{d}_i(t)\mathbf{d}_i^{\mathrm{T}}(t)\right)\mathbf{p}_i(t), \tag{31}$$

$$\hat{\mathbf{p}}(t) = \hat{\mathbf{A}}^{-1}(t)\hat{\mathbf{b}}(t), \tag{32}$$

or by using the pseudoinverse if $\hat{\mathbf{A}}(t)$ is ill-conditioned.

The updated estimate is accepted if the consistency condition is restored:

$$\hat{J}(t) < \tau_J, \qquad \hat{\rho}_{\max}(t) < \tau_\rho. \tag{33}$$

Otherwise, the frame remains observation-inconsistent and the current estimate can be further down-weighted or temporarily discarded, depending on the system policy.

4.3. Configuration Optimization

Configuration optimization is applied when the observations are mutually consistent but the cooperative geometry is weak. In this case, the main limitation does not come from outliers, but from insufficient or anisotropic geometric constraints. Therefore, the objective is to improve the conditioning of LOS intersection by adjusting the UAV configuration.

The detailed pseudocode of the configuration optimization procedure is provided in Appendix A. The functional structure of the configuration optimization module is illustrated in Figure 4.

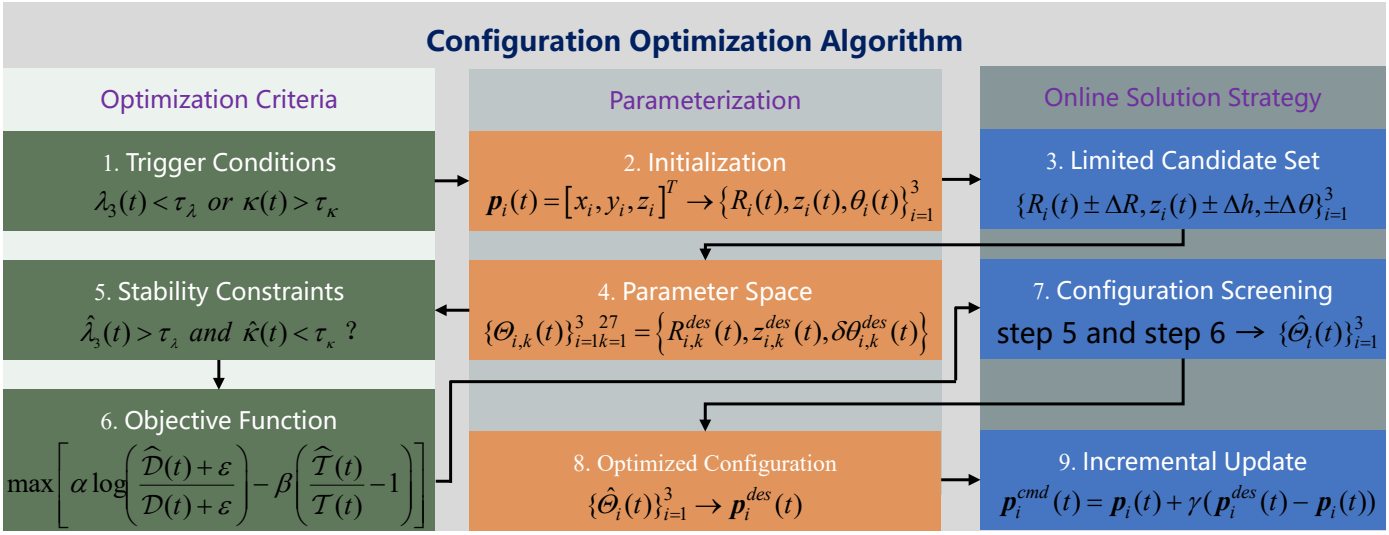


Figure 4. Functional structure of the configuration optimization module.

4.3.1. Optimization Criteria

Configuration optimization is triggered when the current geometry is classified as weak, namely when

$$\lambda_3(t) < \tau_\lambda \quad \text{or} \quad \kappa(t) > \tau_\kappa. \tag{34}$$

The optimization objective combines geometric strengthening and uncertainty reduction. Let $\mathcal{D}(t)$ and $\mathcal{T}(t)$ denote the geometric strength and uncertainty metrics of the current configuration, and let $\hat{\mathcal{D}}(t)$ and $\hat{\mathcal{T}}(t)$ denote the corresponding metrics under a candidate configuration. The objective is defined as

$$\max\left[\alpha\log\left(\frac{\hat{\mathcal{D}}(t)+\varepsilon}{\mathcal{D}(t)+\varepsilon}\right)-\beta\left(\frac{\hat{\mathcal{T}}(t)}{\mathcal{T}(t)}-1\right)\right], \tag{35}$$

where α and β balance geometric strengthening and uncertainty reduction, and ε is a small positive constant introduced for numerical stability.

To avoid switching from one weak configuration to another, the candidate configuration is required to satisfy

$$\hat{\lambda}_3(t) > \tau_\lambda, \qquad \hat{\kappa}(t) < \tau_\kappa. \tag{36}$$

4.3.2. Configuration Parameterization

Let the current estimated target position be

$$\hat{\mathbf{p}}(t) = \left[\hat{x}(t), \hat{y}(t), \hat{z}(t)\right]^{\mathrm{T}}, \tag{37}$$

and let the i-th UAV position be

$$\mathbf{p}_i(t) = \left[x_i(t), y_i(t), z_i(t)\right]^{\mathrm{T}}. \tag{38}$$

The horizontal relative position of the i-th UAV with respect to the current estimate is represented in polar form by

$$R_i(t) = \sqrt{(x_i(t)-\hat{x}(t))^2+(y_i(t)-\hat{y}(t))^2}, \tag{39}$$

$$\theta_i(t) = \operatorname{atan2}\big(y_i(t)-\hat{y}(t),\, x_i(t)-\hat{x}(t)\big). \tag{40}$$

The generated desired position $\mathbf{p}_i^{\mathrm{des}}(t)$ is a full three-dimensional waypoint rather than a planar formation command. Therefore, the configuration optimization simultaneously modifies the horizontal distribution and altitude allocation of the UAV team. In practical deployment, this waypoint can be directly provided to the UAV flight controller as a position reference, allowing coordinated three-dimensional maneuvering toward the desired cooperative configuration.

A candidate configuration is parameterized by the desired horizontal radius, desired altitude, and azimuth correction:

$$\boldsymbol{\Theta}(t) = \left\{R_i^{\mathrm{des}}(t),\, z_i^{\mathrm{des}}(t),\, \delta\theta_i^{\mathrm{des}}(t)\right\}_{i=1}^{3}. \tag{41}$$

The desired position of the i-th UAV is then expressed as

$$\mathbf{p}_i^{\mathrm{des}}(t) = \begin{bmatrix}\hat{x}(t)+R_i^{\mathrm{des}}(t)\cos\big(\theta_i(t)+\delta\theta_i^{\mathrm{des}}(t)\big)\\ \hat{y}(t)+R_i^{\mathrm{des}}(t)\sin\big(\theta_i(t)+\delta\theta_i^{\mathrm{des}}(t)\big)\\ z_i^{\mathrm{des}}(t)\end{bmatrix}. \tag{42}$$

This parameterization provides a compact way to jointly optimize the planar distribution and altitude pattern of the UAV formation around the current target estimate, while generating executable three-dimensional position commands for cooperative maneuvering.

4.3.3. Online Solution Strategy

To ensure online feasibility, a finite candidate set is generated around the current configuration rather than solving a continuous optimization problem at each cycle. Specifically, candidate values are sampled from bounded neighborhoods of the current radii, altitudes, and azimuths:

$$R_i^{\mathrm{des}}(t) \in \{R_i(t) - \Delta R,\ R_i(t),\ R_i(t) + \Delta R\}, \tag{43}$$

$$z_i^{\mathrm{des}}(t) \in \{z_i(t) - \Delta z,\ z_i(t),\ z_i(t) + \Delta z\}, \tag{44}$$

$$\delta\theta_i^{\mathrm{des}}(t) \in \{-\Delta\theta,\ 0,\ +\Delta\theta\}. \tag{45}$$

For each candidate configuration, the corresponding LOS geometry is predicted, the matrix $\hat{\mathbf{A}}(t)$ is constructed, and the objective value is evaluated. The candidate that maximizes the objective while satisfying the stability constraints is selected as the desired configuration.

To avoid oscillatory motion and abrupt maneuver commands, the selected configuration is not executed in a single step. Instead, an incremental update is used:

$$\mathbf{p}_i^{\mathrm{cmd}}(t) = \mathbf{p}_i(t) + \gamma\big(\mathbf{p}_i^{\mathrm{des}}(t) - \mathbf{p}_i(t)\big), \qquad 0 < \gamma < 1, \tag{46}$$

where γ controls the step size of the configuration adjustment.

Through this process, configuration optimization provides a computationally efficient online mechanism for improving cooperative geometry while maintaining smooth UAV motion.

The candidate search is performed over a finite discrete set rather than a continuous optimization space. In the implementation used in this paper, three candidate values are considered for each optimization variable (ΔR, Δz, and $\Delta\theta$), resulting in a total of $3 \times 3 \times 3 = 27$ candidate configurations. For each candidate, only LOS prediction, matrix construction, and geometric metric evaluation are required. Therefore, the computational complexity grows linearly with the number of candidates and remains effectively constant for the current implementation.

On a standard desktop computer (Intel i7-12700 CPU), evaluating all 27 candidates requires less than 1 ms in a Python 3.10.9 simulation, which is substantially shorter than the update period of typical UAV guidance and control loops. Since the optimization is executed by the localization module and only the final desired position is transmitted to the UAVs, no additional computational burden is imposed on the flight controllers.

4.4. Parameter Determination

The parameters of the adaptive optimization framework are determined according to three principles: sensor-noise statistics, localization accuracy requirements, and UAV maneuverability constraints.

First, the observation consistency thresholds are determined from the expected uncertainty of the LOS measurements. For the i-th UAV, the angular noise of the LOS observation is approximated as

$$\sigma_{\theta,i} \approx \frac{\sigma_{\mathrm{px},i}}{f}, \tag{47}$$

where $\sigma_{\mathrm{px},i}$ is the pixel noise standard deviation and f is the focal length in pixels. Given the estimated distance

$$L_i(t) = \|\hat{\mathbf{p}}(t) - \mathbf{p}_i(t)\|, \tag{48}$$

the propagated residual standard deviation is approximated as

$$\sigma_{r,i}(t) = L_i(t)\sigma_{\theta,i}. \tag{49}$$

Using the normalized residual definition introduced in Section 4.2, the individual consistency threshold is selected as

$$\tau_\rho = \sqrt{\chi_2^2(1-\alpha_\rho)}, \tag{50}$$

where α_ρ is the desired false-alarm probability.

For threshold interpretation and experimental implementation, the consistency metric in Section 3 is evaluated in its normalized form:

$$J(t) = \sum_{i=1}^{3} \frac{r_i^2(t)}{\sigma_{r,i}^2(t)}. \tag{51}$$

Since estimating a three-dimensional target position consumes three degrees of freedom, the corresponding global consistency threshold is selected as

$$\tau_J = \chi_3^2(1-\alpha_J), \tag{52}$$

where α_J is the frame-level false-alarm probability.

Second, the geometric stability thresholds are determined according to the required localization accuracy. Under the normalized weighting choice

$$w_i(t) = \frac{1}{\sigma_{r,i}^2(t)}, \tag{53}$$

the localization matrix in Section 2 takes the form

$$\mathbf{F}(t) = \sum_{i=1}^{3} \frac{1}{\sigma_{r,i}^2(t)} \Big(\mathbf{I} - \mathbf{d}_i(t)\mathbf{d}_i^{\mathrm{T}}(t)\Big), \tag{54}$$

which is the normalized information matrix used for threshold interpretation in the experiments. Thus, $\mathbf{F}(t)$ is not a different model, but a noise-normalized special case of the same weighted localization matrix.

The covariance of the localization estimate can then be approximated by $\mathbf{F}^{-1}(t)$. If the maximum allowable one-sigma position uncertainty along the weakest direction is $\sigma_{p,\max}$, the eigenvalue threshold is chosen as

$$\tau_\lambda = \frac{1}{\sigma_{p,\max}^2}. \tag{55}$$

Similarly, if the standard deviation along the weakest direction is allowed to be at most ϱ times that along the strongest direction, the anisotropy threshold is selected as

$$\tau_\kappa = \varrho^2. \tag{56}$$

Third, the adaptive weighting and motion parameters are selected according to robustness and maneuverability requirements. The robust weighting function introduced in Section 4.2 is used to suppress abnormal observations smoothly rather than through hard rejection, and the lower bound $w_{\min}$ is imposed to prevent any LOS observation from being permanently excluded. In configuration optimization, the normalized objective function assigns equal importance to geometric strengthening and uncertainty reduction by default, and $\alpha = \beta = 1$ is used unless a specific task preference is required. The incremental update coefficient γ is selected according to the maximum allowable UAV displacement within one control period so that the generated configuration command remains dynamically feasible.

It should be noted that the remaining parameters used in the simulation studies, including the minimum weight bound $w_{\min}$ and the configuration search step sizes, are engineering parameters rather than theoretically derived constants. Their values were determined through extensive Monte Carlo simulations and repeated validation experiments. Specifically, these parameters were selected according to their ability to provide sufficient discrimination between well-conditioned and degraded configurations, as well as between observation-consistent and observation-inconsistent situations, while maintaining stable optimization behavior and acceptable computational cost.

Because the statistical characteristics of sensor noise, target distance, UAV maneuverability, and operational environments may vary across different applications, these parameters should be regarded as scenario-dependent design parameters. In practical deployments, they can be re-calibrated using the same statistical analysis procedure described above. Therefore, the proposed framework does not rely on a unique parameter set but rather on a parameter selection methodology based on uncertainty statistics, geometric conditioning requirements, and platform constraints.

In summary, the adaptive optimization framework developed in this section jointly addresses observation inconsistency and weak geometry. Adaptive weighting improves robustness against unreliable LOS measurements, while configuration optimization actively improves the conditioning of the cooperative geometry. Together, they provide the online correction mechanisms required by the reliability assessment developed in Section 3.

5. Simulation Results and Analysis

5.1. System Setup and Simulation Environment

To validate the proposed adaptive optimization framework for bearing-only three-UAV cooperative localization, a modular simulation system is constructed, consisting of five functional modules and a simulation environment, as shown in Figure 5.

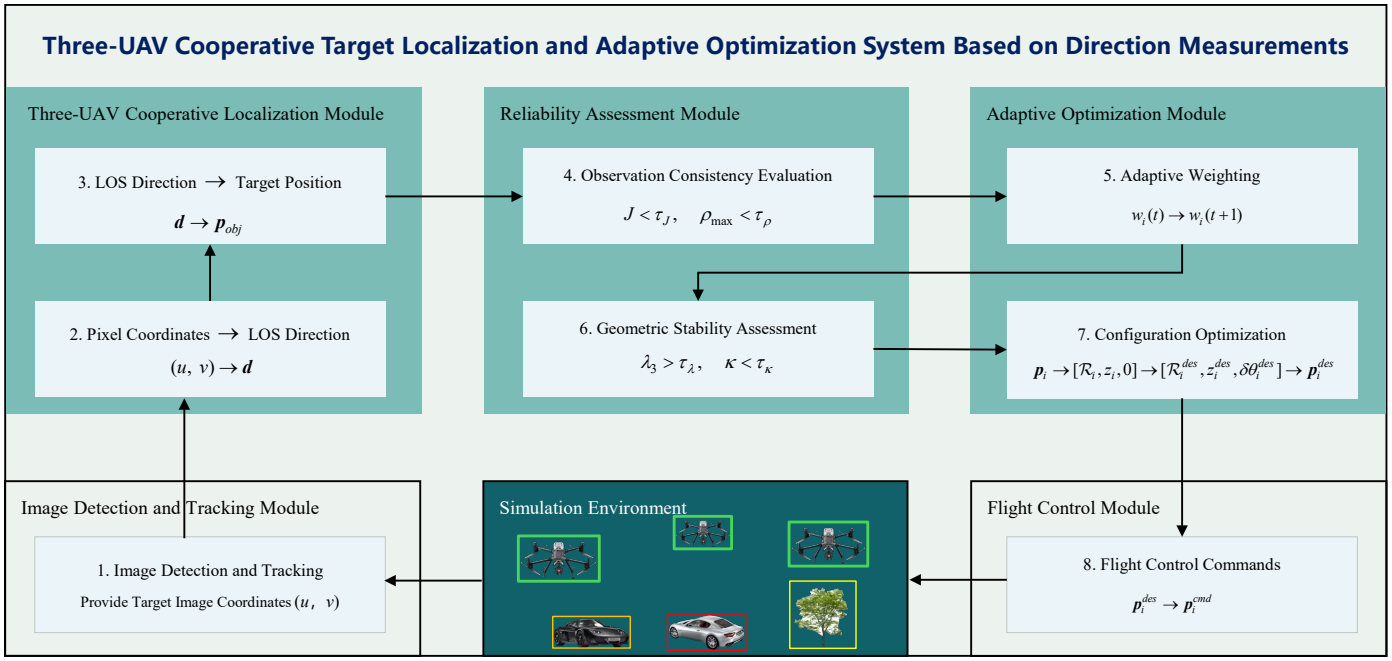


Figure 5. Three-UAV cooperative target localization and adaptive optimization system. Green boxes denote the localization UAVs, the red box denotes the observed target, the orange boxes denote the fake targets, the yellow box denotes the occluder, and the arrows indicate the sequence of the process flow.

The simulation environment includes three UAVs, one target, one interference source for false detection, and one occluder. To emulate realistic sensing conditions, each UAV is equipped with a monocular camera characterized by different pixel noise levels and detection confidences, as listed in Table 1.

Table 1. Noise and confidence settings of the three UAV cameras.

UAV Camera	Pixel Noise Standard Deviation (px)	Detection Confidence
1	0.8	0.9
2	1.6	0.7
3	3.2	0.5

The camera intrinsic matrix is set as

$$\mathbf{K} = \begin{bmatrix} 600 & 0 & 320 \\ 0 & 600 & 240 \\ 0 & 0 & 1 \end{bmatrix}. \tag{57}$$

The parameter values used in the following simulations are determined according to the procedure described in Section 4.4. The observation consistency thresholds were set as $\tau_\rho = 3.0$ and $\tau_J = 7.81$, corresponding to the normalized individual residual bound and the 95% chi-square bound for the global consistency metric, respectively. The geometric stability thresholds were set as $\tau_\lambda = 9.0\ \mathrm{m}^{-2}$ and $\tau_\kappa = 16$, which correspond to a maximum one-sigma uncertainty of approximately 0.33 m along the weakest direction and a maximum uncertainty anisotropy ratio of 4. For adaptive weighting, the lower weight bound was set to $w_{\min} = 0.10$. For configuration optimization, $\alpha = \beta = 1$ was adopted after normalization, and the incremental update coefficient was set to $\gamma = 0.25$. The desired horizontal radius was $R_{\mathrm{des}} = 15$ m, with candidate search steps of $\Delta R = 3$ m, $\Delta\theta = 20^\circ$, and $\Delta z = 1$ m.

The system pipeline is as follows: the detection and tracking module outputs image coordinates (u, v); the localization module converts them into LOS vectors and estimates the target position using the model in Section 2; the reliability assessment module computes the geometric and observation consistency metrics; the adaptive optimization module updates the weights and configuration; and the flight control module executes the resulting motion commands.

5.2. Validation of Reliability Metrics

5.2.1. Geometric Stability Metrics

Six representative configurations are designed for geometric stability evaluation, as illustrated in Figure 6.

As shown in Table 2, Configurations 1–3 are all classified as geometrically stable because they satisfy both $\lambda_3(t) > \tau_\lambda$ and $\kappa(t) < \tau_\kappa$. Nevertheless, the metrics still reveal clear differences in configuration quality. From Configuration 1 to Configuration 3, $\log \mathcal{D}(t)$ decreases, $\lambda_3(t)$ decreases, and $\mathcal{T}(t)$ increases, indicating a gradual reduction in geometric information and an increase in localization uncertainty.

Configurations 4–6 further demonstrate different types of geometric degradation. Configuration 4 maintains a balanced angular distribution but has a larger observation distance, leading to $\lambda_3(t) = 8.5263 < \tau_\lambda$ while $\kappa(t)$ remains below τ_κ. This indicates insufficient overall information strength. Configuration 5 has a compressed angular distribution, resulting in $\kappa(t) = 18.1345 > \tau_\kappa$ while $\lambda_3(t)$ remains above the threshold, indicating strong anisotropy of localization uncertainty. Configuration 6 combines both long-range observation and angular compression, causing both $\lambda_3(t) < \tau_\lambda$ and $\kappa(t) > \tau_\kappa$. These results

verify that the proposed geometric metrics can not only detect degraded geometry but also distinguish different degradation mechanisms.

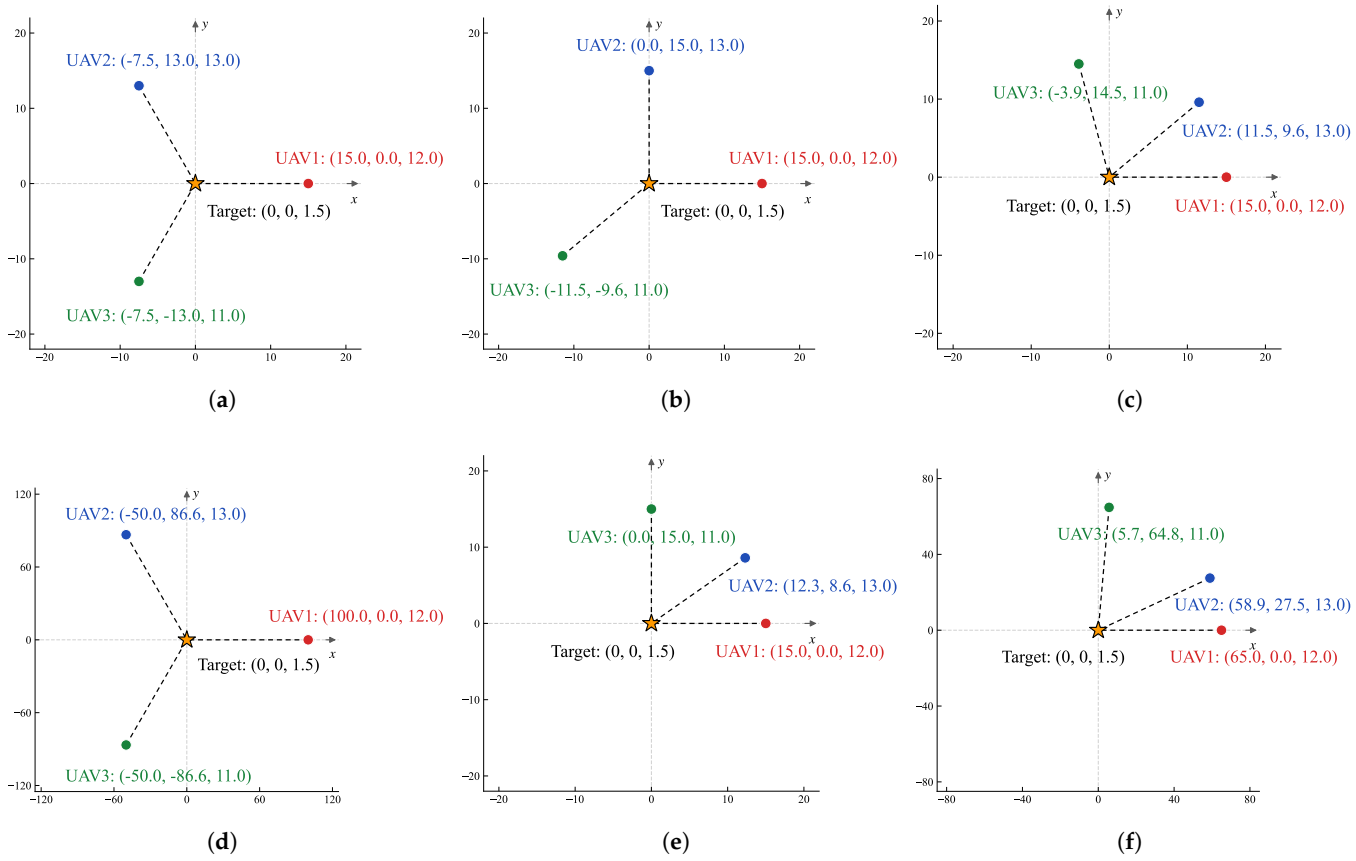


Figure 6. Illustration of six cooperative UAV configurations used for geometric stability evaluation. (**a**) Configuration 1: Balanced Normal Configuration. (**b**) Configuration 2: Mildly Skewed Normal Configuration. (**c**) Configuration 3: Near−Threshold but Stable Configuration. (**d**) Configuration 4: Long−Range Balanced Degraded Configuration. (**e**) Configuration 5: One−Sided Clustered Configuration. (**f**) Configuration 6: Long−Range and Angularly Compressed Configuration.

Table 2. Comparison of geometric stability indicators under six configurations.

Configuration	$\log \mathcal{D}(t)$	$\kappa(t)$	$\lambda_3(t)$	$\mathcal{T}(t)$	RMSE (m)
1	20.6460	5.3945	331.0209	0.0042	0.06
2	20.5355	6.1966	288.6319	0.0046	0.07
3	19.7720	15.0695	121.9862	0.0093	0.12
4	10.2334	7.2004	8.5263	0.1524	0.45
5	19.5997	18.1345	101.4756	0.0110	0.18
6	11.8708	19.5794	7.3258	0.1508	0.60

5.2.2. Observation Consistency Metrics

Using a well-conditioned configuration, three observation scenarios are considered: consistent observations, false detection, and occlusion-induced drift, as shown in Figure 7. The false target is introduced solely to emulate abnormal LOS observations that may arise from perception errors such as false detections, target misassociations, or tracking failures, rather than to address false-target identification itself. For observation consistency evaluation, 1000 Monte Carlo trials are conducted under each scenario. In each trial, pixel noise is randomly sampled, and the normalized maximum residual $\rho_{\max}(t)$ and the consistency metric $J(t)$ are averaged over all trials.

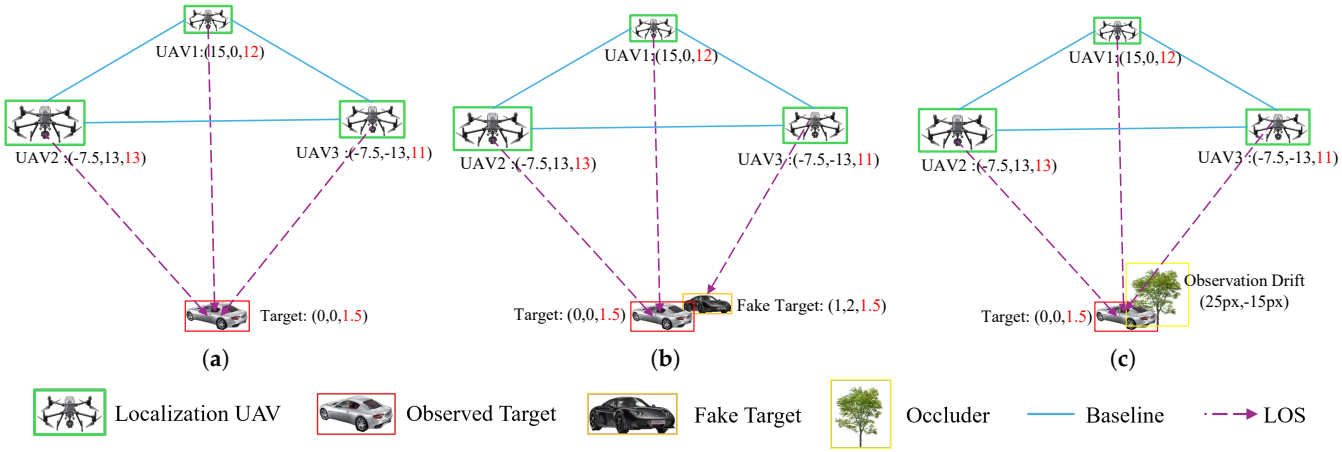


Figure 7. Illustration of three observation scenarios. (**a**) Scenario 1: Consistent Observations. (**b**) Scenario 2: False Detection on UAV3. (**c**) Scenario 3: Occlusion−Induced Drift on UAV3.

As shown in Table 3, the consistency metrics remain low under consistent observations, with $\rho_{\max} = 1.3657$ and $J = 3.0032$, both below the predefined thresholds $\tau_\rho = 3.0$ and $\tau_J = 7.81$. The corresponding inconsistency rate is 5.44%, which is consistent with the expected false-alarm level of the threshold design.

Table 3. Comparison of observation consistency metrics in three observation scenarios.

Scenario	Mean: $\rho_{\max}$	Mean: J	Inconsistency Rate
1	1.3657	3.0032	5.44%
2	10.5090	119.0851	100.00%
3	7.7282	69.6348	100.00%

In contrast, both abnormal observation scenarios show significant increases in the consistency metrics. Under UAV3 false detection, $\rho_{\max}$ and J increase to 10.5090 and 119.0851, respectively. Under UAV3 occlusion-induced drift, the two metrics increase to 7.7282 and 69.6348, respectively. In both cases, the inconsistency rate reaches 100%, indicating that the proposed observation consistency metrics can effectively detect false detections and occlusion-induced measurement drift.

5.3. Validation of the Adaptive Optimization Framework

Four test scenarios are considered for validating the adaptive optimization framework: well-conditioned geometry with consistent observations, well-conditioned geometry with inconsistent observations, degraded geometry with consistent observations, and degraded geometry with inconsistent observations, as illustrated in Figure 8.

Tables 4–8 present the ablation and comparative evaluation results under four representative scenarios. The baseline corresponds to the unweighted point-to-line least-squares solution, which is equivalent to the classical LS/intersection localization method [35] under the current formulation, while v1 corresponds to its weighted least-squares counterpart (WLS) [35]. Huber-WLS is additionally included as a representative robust localization method based on residual reweighting. The proposed framework is evaluated through two progressive variants: v2 incorporates adaptive weighting on top of WLS, whereas v3 further integrates configuration optimization. Therefore, the performance differences between v1, v2, and v3 directly reflect the contributions of the proposed reliability-aware adaptive weighting and geometry optimization mechanisms rather than changes in the underlying geometric localization solver.

To provide a more comprehensive evaluation, the results are reported using multiple statistical indicators, including mean localization error, RMSE, standard deviation, maximum error, and 95% confidence intervals. Furthermore, Figure 9 presents box plots of the localization error distributions, enabling a visual comparison of error dispersion, robustness, and outlier behavior among different methods.

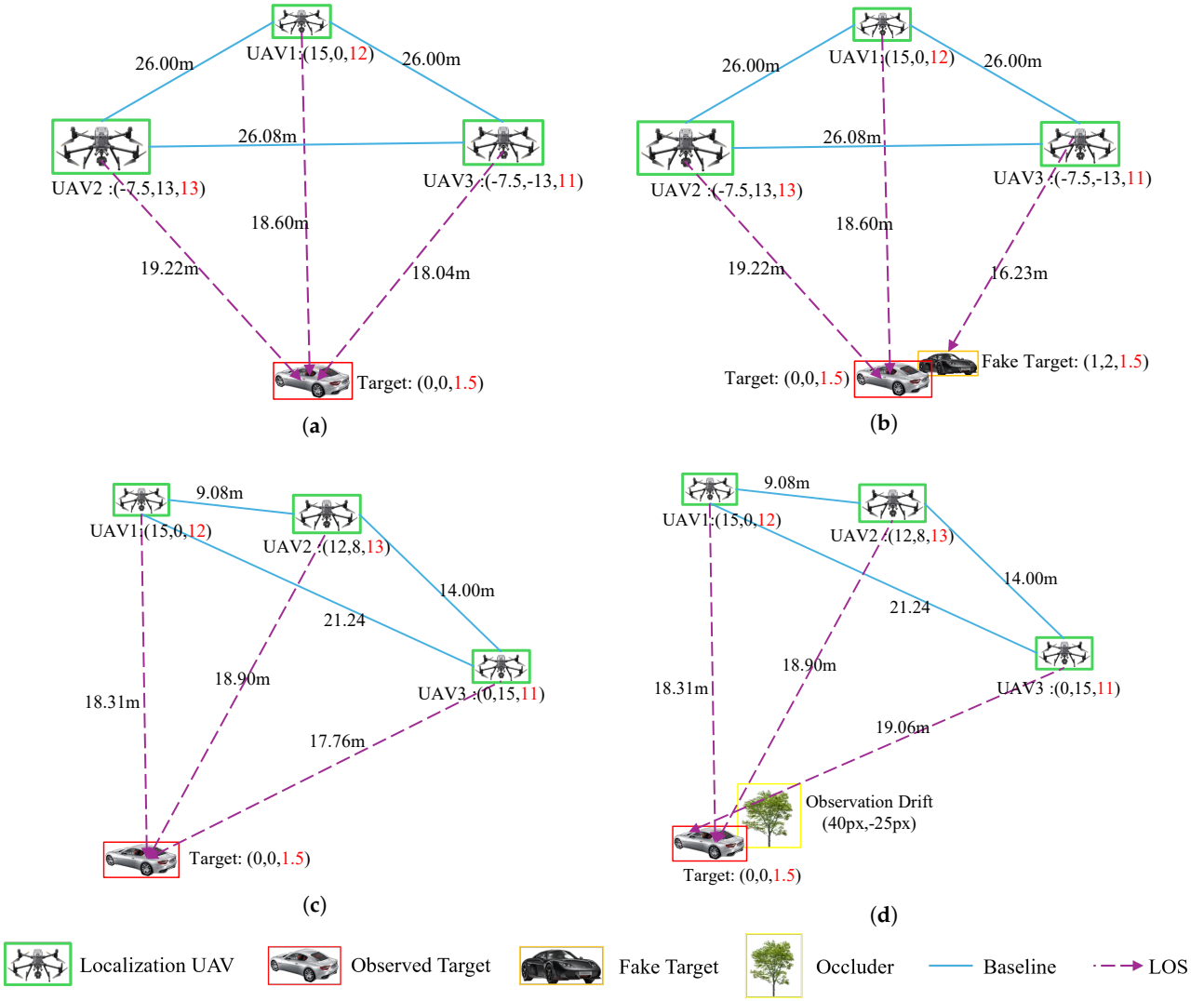


Figure 8. Illustration of four test scenarios for adaptive optimization validation. (**a**) Scenario 1: well−conditioned geometry with consistent observations. (**b**) Scenario 2: well−conditioned geometry with UAV3 false detection. (**c**) Scenario 3: degraded geometry with consistent observations. (**d**) Scenario 4: degraded geometry with UAV3 occlusion drift.

Table 4. Ablation and comparative evaluation under four scenarios (Mean Error, ✓ indicates the usage of this model).

Method	Weighted	Weight Adaptation	Configuration Optimization	Mean Error in Scenario 1 (m)	Mean Error in Scenario 2 (m)	Mean Error in Scenario 3 (m)	Mean Error in Scenario 4 (m)
Baseline				0.071	0.545	0.388	0.666
v1 (WLS)	✓			0.061	0.449	0.355	0.711
v2	✓	✓		0.061	0.260	0.355	0.500
v3	✓	✓	✓	0.061	0.260	0.081	0.280
Huber				0.070	0.245	0.373	0.410

Table 5. Ablation and comparative evaluation under four scenarios (RMSE, ✓ indicates the usage of this model).

Method	Weighted	Weight Adaptation	Configuration Optimization	RMSE in Scenario 1 (m)	RMSE in Scenario 2 (m)	RMSE in Scenario 3 (m)	RMSE in Scenario 4 (m)
Baseline				0.078	0.548	0.481	0.865
v1 (WLS)	✓			0.067	0.417	0.440	0.937
v2	✓	✓		0.067	0.290	0.440	0.610
v3	✓	✓	✓	0.067	0.290	0.108	0.390
Huber				0.077	0.267	0.483	0.521

Table 6. Ablation and comparative evaluation under four scenarios (Standard Deviation, ✓ indicates the usage of this model).

Method	Weighted	Weight Adaptation	Configuration Optimization	Std in Scenario 1 (m)	Std in Scenario 2 (m)	Std in Scenario 3 (m)	Std in Scenario 4 (m)
Baseline				0.032	0.051	0.285	0.552
v1 (WLS)	✓			0.028	0.043	0.260	0.611
v2	✓	✓		0.028	0.070	0.260	0.420
v3	✓	✓	✓	0.028	0.070	0.071	0.250
Huber				0.032	0.107	0.283	0.321

Table 7. Ablation and comparative evaluation under four scenarios (Maximum Error, ✓ indicates the usage of this model).

Method	Weighted	Weight Adaptation	Configuration Optimization	Max Error in Scenario 1 (m)	Max Error in Scenario 2 (m)	Max Error in Scenario 3 (m)	Max Error in Scenario 4 (m)
Baseline				0.22	0.72	1.85	4.20
v1 (WLS)	✓			0.23	0.60	1.75	3.45
v2	✓	✓		0.20	0.65	1.80	2.10
v3	✓	✓	✓	0.20	0.55	1.06	1.40
Huber				0.23	0.75	1.75	2.90

Table 8. Ablation and comparative evaluation under four scenarios (CI95, ✓ indicates the usage of this model).

Method	Weighted	Weight Adaptation	Configuration Optimization	CI95 in Scenario 1 (m)	CI95 in Scenario 2 (m)	CI95 in Scenario 3 (m)	CI95 in Scenario 4 (m)
Baseline				0.071 ± 0.003	0.545 ± 0.004	0.388 ± 0.025	0.666 ± 0.048
v1 (WLS)	✓			0.061 ± 0.002	0.449 ± 0.004	0.355 ± 0.023	0.711 ± 0.054
v2	✓	✓		0.061 ± 0.002	0.260 ± 0.006	0.355 ± 0.023	0.500 ± 0.037
v3	✓	✓	✓	0.061 ± 0.002	0.260 ± 0.006	0.081 ± 0.006	0.280 ± 0.022
Huber				0.070 ± 0.003	0.245 ± 0.009	0.373 ± 0.025	0.410 ± 0.028

As shown in Tables 4–8 and Figure 9, the proposed adaptive optimization framework improves localization performance under different degradation conditions in a complementary manner.

In Scenario 1, where both the observation consistency and geometric configuration are favorable, all weighted methods achieve similar localization performance. The mean error decreases from 0.071 m for the baseline LS solution to 0.061 m for WLS, while the adaptive weighting and configuration optimization modules provide no additional improvement. This behavior is expected because neither observation inconsistency nor geometric degradation is present, and therefore no corrective action is required.

In Scenario 2, where abnormal observations are introduced while maintaining a favorable geometry, the mean error decreases from 0.545 m for the baseline method to

0.449 m for WLS and further to 0.260 m after enabling adaptive weighting. The comparable performance of v2 and v3 confirms that observation inconsistency is the dominant error source in this scenario and that configuration optimization is not activated. Huber-WLS achieves a slightly lower mean error of 0.245 m due to its strong residual-based outlier suppression capability. However, unlike the proposed method, it does not explicitly evaluate observation reliability and therefore cannot address geometric degradation.

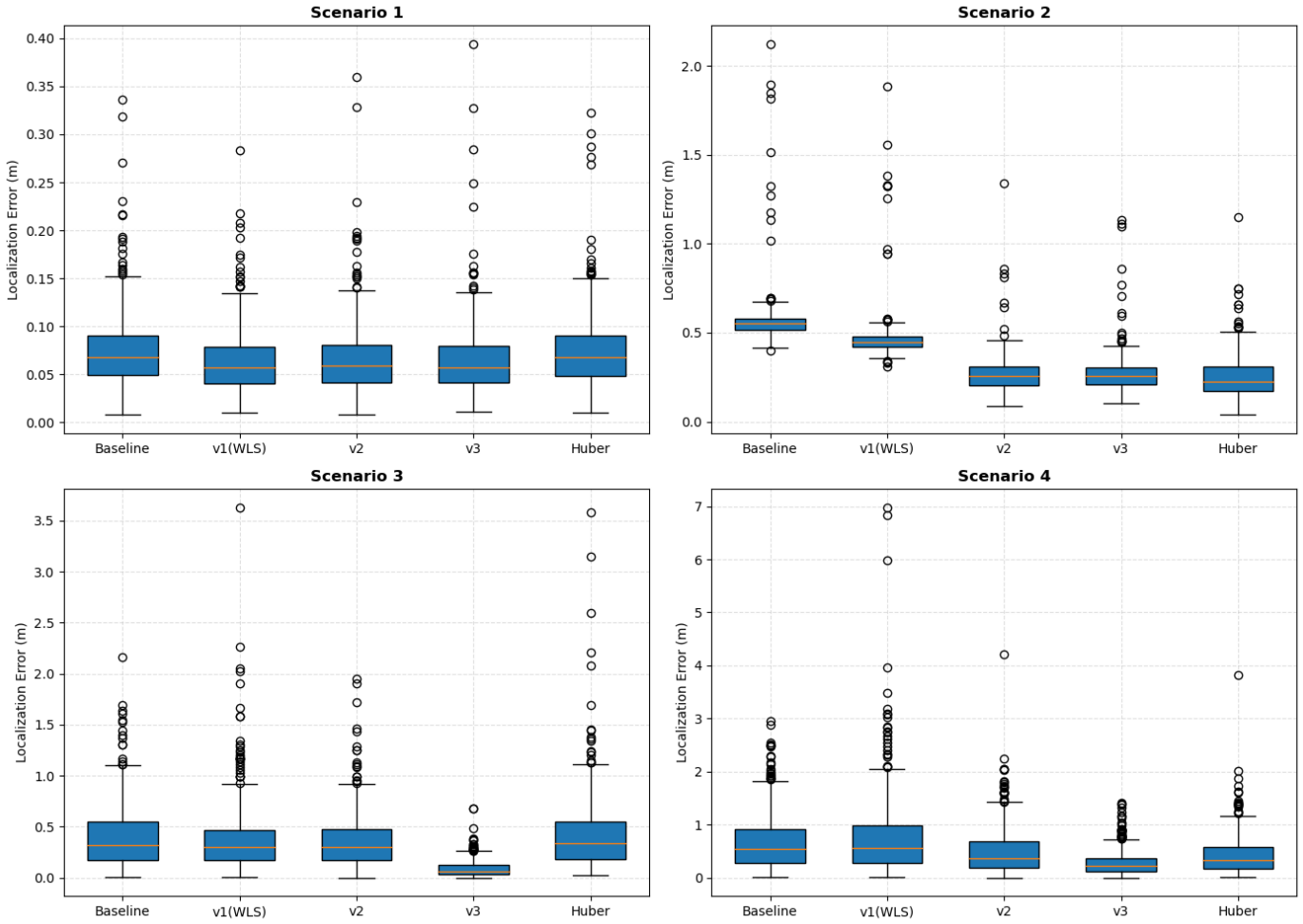


Figure 9. Ablation and comparative evaluation under four scenarios (Boxplot). The upper and lower bases of the rectangle (box) are set at the 1st and 3rd quartile. The line within the box represents the median. The open circles represent outliers.

In Scenario 3, where the primary challenge is geometric degeneration rather than observation inconsistency, adaptive weighting provides almost no additional benefit compared with WLS, as reflected by the identical mean errors of 0.355 m for v1 and v2. In contrast, configuration optimization significantly improves localization accuracy, reducing the mean error to 0.081 m and the RMSE from 0.440 m to 0.108 m. The box plot in Figure 9 also shows a substantial reduction in error dispersion and outliers, demonstrating the effectiveness of active geometry enhancement under near-collinear configurations.

In Scenario 4, where both observation inconsistency and geometric degradation coexist, the proposed full framework achieves the best overall performance. The mean error is reduced from 0.711 m for WLS to 0.500 m after adaptive weighting and further to 0.280 m after configuration optimization. Compared with Huber-WLS, which achieves a mean error of 0.410 m, the proposed method exhibits both lower average error and smaller error dispersion because it simultaneously improves observation reliability and geometric condi-

tioning. This result demonstrates that adaptive weighting and configuration optimization address complementary failure modes and jointly provide robust localization performance under challenging operating conditions.

Furthermore, the standard deviation, maximum error, confidence intervals, and boxplot distributions consistently support the same conclusions. The proposed framework not only improves average localization accuracy but also reduces error dispersion and limits large-error occurrences, indicating improved robustness and statistical stability across different localization scenarios.

6. Discussion

The simulation results show that the framework can effectively distinguish between observation inconsistency and weak geometry, and activate the appropriate corrective strategy accordingly. Adaptive weighting is particularly effective when abnormal LOS observations occur, whereas configuration optimization mainly improves localization performance under degraded geometry. The two mechanisms are therefore complementary: adaptive weighting enhances robustness against unreliable measurements, while configuration optimization improves the intrinsic observability of the cooperative geometry.

From a computational perspective, the proposed method is suitable for online implementation in the three-UAV case. The localization step only requires constructing and solving a 3×3 linear system, and the reliability assessment involves residual computation and eigenvalue analysis of the same low-dimensional matrix. Additional computation mainly arises from the candidate screening process in the configuration optimization module. Since each candidate only requires LOS prediction and geometric metric evaluation, the overall computational burden remains limited for the current three-UAV setting. However, as the number of UAVs or candidate configurations increases, the search space may grow rapidly. In such cases, more efficient candidate selection, hierarchical screening, or distributed optimization strategies may be required.

For experimental evaluation, the baseline and weighted variants in Table 4 already correspond to the most directly comparable classical single-frame angle-only localization methods, namely LS/intersection localization and WLS, respectively. Therefore, the purpose of the ablation study is not to replace the underlying geometric solver, but to quantify the performance gains introduced by the reliability-aware adaptive weighting and configuration optimization mechanisms. Recent multi-UAV bearing-only studies often focus on multi-frame target tracking, distributed filtering, or tracking–control integration, which are not fully aligned with the present scenario-based cooperative localization setting. For this reason, the experimental comparison in this paper emphasizes self-consistent classical baselines under the same four test scenarios.

The current framework is developed for a three-UAV cooperative localization structure. Three UAVs constitute a minimal robust configuration for bearing-only 3D localization, because they provide redundant LOS constraints beyond the ideal two-ray intersection case. Nevertheless, the present formulation does not explicitly address large-scale UAV swarms. For systems involving more than three UAVs, the proposed framework could be extended by selecting reliable UAV subsets, jointly fusing all available LOS observations, or decomposing the system into multiple three-UAV localization units. Such extensions may further improve robustness, but they will also introduce additional challenges related to communication load, synchronization, and distributed decision-making.

A key limitation lies in the idealized sensing and navigation assumptions adopted in the simulations, where EO/IR camera gimbal angle errors, IMU errors, and GPS errors were treated as bias or uniform values. In practice, these errors vary among UAVs during swarm flight and should be modeled as variances rather than fixed biases. Attitude estimation

errors, for instance, introduce angular deviations into the LOS vectors that differ across UAVs in both magnitude and direction. An attitude error of only 1° produces an angular deviation of approximately 0.017 rad, which translates into a target position error of about 0.17 m at a 10 m distance and more than 0.8 m at 50 m. Because the actual error varies from UAV to UAV, the resulting position error depends on the specific error distribution across the swarm and cannot be characterized by a single systematic bias. Similar considerations apply to GPS/INS positioning errors and camera intrinsic calibration errors, where inter-UAV variability, temporal correlation, and optical-axis misalignment can all generate observation deviations that may appear geometrically self-consistent within a subset of UAVs while still producing biased estimates. Consequently, the reliability indicators introduced in this paper should be interpreted as measures of geometric observability and internal consistency, rather than direct estimators of absolute localization accuracy. A meaningful future direction is to jointly model random observation noise and the variance characteristics of sensor errors (pose uncertainty, calibration, synchronization) within the localization covariance, thereby enabling more comprehensive and UAV-specific reliability assessment. A practical challenge is that obtaining reliable per-UAV error distributions for these sensor sources is often difficult in field deployments.

Several other limitations point to concrete research directions. Extending the three-UAV framework to larger teams can provide redundancy, but it also introduces communication overhead, synchronization requirements, and distributed decision-making complexity. A promising direction is to develop scalable, distributed reliability metrics and hierarchical configuration optimization, though achieving consensus under real-time and bandwidth constraints remains a substantial difficulty. For highly maneuvering targets, integrating the proposed frame-wise reliability assessment with recursive Bayesian filters (e.g., EKF) is natural, but propagating the reliability indicators over time while maintaining real-time performance is non-trivial. Incorporating realistic flight constraints—such as vehicle dynamics, obstacle avoidance, no-fly zones, and energy limits—transforms the current geometric optimization into a constrained cooperative planning problem, which is significantly more challenging to solve online. Finally, transitioning from simulation to real-world validation will require quantifying the impact of UAV pose uncertainty, camera calibration errors, and environmental disturbances. The central difficulty lies in establishing a unified uncertainty propagation framework that fuses random measurement noise with systematic sensor errors, which will be a key focus of subsequent flight experiments.

7. Conclusions

This paper presented an adaptive optimization framework for three-UAV cooperative bearing-only localization that addresses both observation anomalies and degraded geometry. By combining geometric stability indicators with observation consistency metrics, the framework identifies weak configurations and abnormal observations online, and triggers adaptive weighting and configuration optimization accordingly. Simulation results under four representative scenarios demonstrate consistent improvements in localization accuracy and robustness. Under observation inconsistency, adaptive weighting reduces the mean localization error from 0.545 m to 0.260 m; under degraded geometry, configuration optimization reduces it from 0.355 m to 0.081 m; and under combined degradation, the full framework reduces it from 0.711 m to 0.280 m. Statistical analysis of RMSE, standard deviation, maximum error, confidence intervals, and error distributions confirms that the proposed method improves both accuracy and stability by reducing error dispersion and suppressing large-error occurrences. Overall, the framework provides a computationally efficient and reliability-aware solution for cooperative UAV localization.

Future work will focus on incorporating systematic error sources—including UAV pose uncertainty and camera calibration bias—as well as validating the framework through real-flight experiments.

Author Contributions: Conceptualization, K.L. and H.S.; methodology, K.L., H.S., Z.R. and M.W.; software, K.L.; validation, K.L., M.W. and C.C.; formal analysis, K.L., Z.R. and M.W.; investigation, H.S.; resources, C.C., Z.R. and J.Y.; data curation, H.S.; writing—original draft preparation, K.L. and M.W.; writing—review and editing, K.L., Z.R. and J.Y.; visualization, K.L. and H.S.; supervision, M.W. and C.C.; project administration, M.W.; funding acquisition, Z.R., M.W. and C.C. All authors have read and agreed to the published version of the manuscript.

Funding: This work was supported by the Major National Science and Technology Special Project of China (Grant No. 2024ZD1002604), Excellent Youth Science Fund Project (Over-seas) of Shandong Province, China (Grant No. 2023HWYQ-029), Youth Project of Natural Science Foundation of Shandong Province, China (Grant No. ZR2023QE127), Guangdong Basic and Applied Basic Research Foundation (Grant No. 2023A1515110509) and Gansu Province Postdoctoral Fund (Grant No. 24JRRA219).

Data Availability Statement: The original contributions presented in this study are included in the article. Further inquiries can be directed to the corresponding author.

Conflicts of Interest: Authors Kangkang Li, Haodong Sun and Jianping Yuan were employed by the company Weiqiao-UCAS (Binzhou) Science and Technology Co., Ltd. Author Mengbi Wang was employed by the company Weiqiao-UCAS (Beijing) Science and Technology Co., Ltd. The remaining authors declare that the research was conducted in the absence of any commercial or financial relationships that could be construed as a potential conflict of interest.

Abbreviations

The following abbreviations are used in this manuscript:

UAV	Unmanned Aerial Vehicle
LOS	Line of Sight
LS	Least-Squares
WLS	Weighted Least-Squares

Appendix A

This appendix provides the detailed pseudocode of the configuration optimization procedure described in Section 4.3. The purpose of including this algorithm is to clarify the online decision logic, candidate generation process, feasibility screening, and incremental update strategy used in the proposed adaptive optimization framework. Compared with the main text, the appendix emphasizes implementation flow rather than theoretical derivation, while keeping the notation fully consistent with Sections 3 and 4.

Algorithm A1 Configuration Optimization Algorithm

Input:
Observation consistency metrics $J(t)$ and $\rho_{\max}(t)$
Geometric stability metrics $\lambda_3(t)$, $\kappa(t)$, $\mathcal{D}(t)$, and $\mathcal{T}(t)$
Thresholds τ_J, τ_ρ, τ_λ, and τ_κ
Current target estimate $\hat{\mathbf{p}}(t)$
Current UAV positions $\{\mathbf{p}_i(t)\}_{i=1}^3$
Current configuration parameters $\{R_i(t), z_i(t), \theta_i(t)\}_{i=1}^3$
Search steps ΔR, Δz, and $\Delta\theta$
Objective weights α and β, smoothing coefficient γ, and numerical constant ε
Output:
Updated UAV position commands $\{\mathbf{p}_i^{\mathrm{cmd}}(t)\}_{i=1}^3$

Algorithm A1 *Cont.*

Initialize $\mathbf{p}_i^{\mathrm{cmd}}(t) \leftarrow \mathbf{p}_i(t)$ for $i = 1, 2, 3$
if $J(t) \geq \tau_J$ **or** $\rho_{\max}(t) \geq \tau_\rho$ **then**
  return $\{\mathbf{p}_i^{\mathrm{cmd}}(t)\}_{i=1}^3$ ▷ No configuration update under observation inconsistency
end if
if $\lambda_3(t) \geq \tau_\lambda$ **and** $\kappa(t) \leq \tau_\kappa$ **then**
  return $\{\mathbf{p}_i^{\mathrm{cmd}}(t)\}_{i=1}^3$ ▷ Current geometry is already satisfactory
end if
for $i = 1$ to 3 **do**
  $\mathcal{R}_i \leftarrow \{R_i(t) - \Delta R,\ R_i(t),\ R_i(t) + \Delta R\}$
  $\mathcal{Z}_i \leftarrow \{z_i(t) - \Delta z,\ z_i(t),\ z_i(t) + \Delta z\}$
  $\mathcal{A}_i \leftarrow \{-\Delta\theta,\ 0,\ +\Delta\theta\}$
end for
Construct the candidate parameter set

$$\mathcal{C} = \left\{ \left(R_i^{\mathrm{des}}, z_i^{\mathrm{des}}, \delta\theta_i^{\mathrm{des}}\right)_{i=1}^3 \,\middle|\, R_i^{\mathrm{des}} \in \mathcal{R}_i,\ z_i^{\mathrm{des}} \in \mathcal{Z}_i,\ \delta\theta_i^{\mathrm{des}} \in \mathcal{A}_i \right\}.$$

Set $s^\star \leftarrow -\infty$
Set $\{\mathbf{p}_i^\star(t)\}_{i=1}^3 \leftarrow \{\mathbf{p}_i(t)\}_{i=1}^3$
for all $\mathbf{c} \in \mathcal{C}$ **do**
  Convert $\mathbf{c}$ into desired UAV positions $\{\mathbf{p}_i^{\mathrm{des}}(t)\}_{i=1}^3$ using the parameterization in Section 4.3
  Predict the corresponding LOS geometry
  Compute $\hat{\lambda}_3(t)$, $\hat{\kappa}(t)$, $\hat{\mathcal{D}}(t)$, and $\hat{\mathcal{T}}(t)$
  if $\hat{\lambda}_3(t) > \tau_\lambda$ **and** $\hat{\kappa}(t) < \tau_\kappa$ **then**
    Evaluate the candidate score

$$s(\mathbf{c}) = \alpha \log\left(\frac{\hat{\mathcal{D}}(t) + \varepsilon}{\mathcal{D}(t) + \varepsilon}\right) - \beta\left(\frac{\hat{\mathcal{T}}(t)}{\mathcal{T}(t)} - 1\right)$$

    if $s(\mathbf{c}) > s^\star$ **then**
      $s^\star \leftarrow s(\mathbf{c})$
      $\{\mathbf{p}_i^\star(t)\}_{i=1}^3 \leftarrow \{\mathbf{p}_i^{\mathrm{des}}(t)\}_{i=1}^3$
    end if
  end if
end for
for $i = 1$ to 3 **do**
  $\mathbf{p}_i^{\mathrm{cmd}}(t) \leftarrow \mathbf{p}_i(t) + \gamma\left(\mathbf{p}_i^\star(t) - \mathbf{p}_i(t)\right)$
end for
return $\{\mathbf{p}_i^{\mathrm{cmd}}(t)\}_{i=1}^3$

References

1. Zhu, H.Y.; Lin, C.Z.; Liu, G.Q.; Wang, D.N.; Qin, S.; Li, A.J.; Xu, J.-L.; He, Y. Intelligent agriculture: Deep learning in UAV-based remote sensing imagery for crop diseases and pests detection. *Front. Plant Sci.* **2024**, *15*, 1435016. [CrossRef] [PubMed]
2. He, Y.; Huang, C.; Yu, F.-R.; Liu, Z.; Zhou, G. Quantum reinforcement learning for cognitive radio-assisted UAV traffic offloading. *IEEE Trans. Veh. Technol.* **2025**, *74*, 14620–14631. [CrossRef]
3. Lyu, C.; Lin, S.; Lynch, A.; Zou, Y.; Liarokapis, M. UAV-based deep learning applications for automated inspection of civil infrastructure. *Autom. Constr.* **2025**, *177*, 106285. [CrossRef]
4. Surman, K.; Lockey, D. Unmanned aerial vehicles and pre-hospital emergency medicine. *Scand. J. Trauma Resusc. Emerg. Med.* **2024**, *32*, 9. [CrossRef] [PubMed]
5. Hou, Z.Q.; Zheng, Z.; Gu, Y.Q.; Zhang, C.H.; Li, H.J. UAV high speed target reconnaissance and deblurring. *IEEE Access* **2025**, *13*, 72620–72632. [CrossRef]
6. Ding, H.; Zhu, Y.; Map, R. Strike Target Assignment for Multi-UAV Cooperative Missions in Uncertain Environments. In Proceedings of the 2025 5th International Conference on Electronic Information Engineering and Computer Technology (EIECT), Jiangmen, China, 24–26 October 2025.
7. Zhang, J.; Chen, L.; Gao, Z.J.; Duo, Y.X. Low-Altitude Unmanned Aerial Vehicle Technology: Current Status and Prospects. *Strateg. Study Chin. Acad. Eng.* **2025**, *27*, 73–85. [CrossRef]
8. Oshman, Y.; Davidson, P. Optimization of observer trajectories for bearings-only target localization. *IEEE Trans. Aerosp. Electron. Syst.* **1999**, *35*, 892–902. [CrossRef]

9. Wang, Z.; Luo, J.A.; Zhang, X.P. A novel location-penalized maximum likelihood estimator for bearing-only target localization. *IEEE Trans. Signal Process.* **2012**, *60*, 6166–6181. [CrossRef]
10. Luo, J.A.; Shao, X.H.; Peng, D.L.; Zhang, X.P. A novel subspace approach for bearing-only target localization. *IEEE Sens. J.* **2019**, *19*, 8174–8182. [CrossRef]
11. He, L.; Gong, P.; Zhang, X.; Wang, Z. The bearing-only target localization via the single UAV: Asymptotically unbiased closed-form solution and path planning. *IEEE Access* **2019**, *7*, 153592–153604. [CrossRef]
12. Li, J.; Ning, Z.; He, S.; Lee, C.H.; Zhao, S. Three-dimensional bearing-only target following via observability-enhanced helical guidance. *IEEE Trans. Robot.* **2022**, *39*, 1509–1526.
13. Sun, P.; Tong, S.; Qin, K.; Luo, Z.; Lin, B.; Shi, M. Low-Cost Real-Time Remote Sensing and Geolocation of Moving Targets via Monocular Bearing-Only Micro UAVs. *Remote Sens.* **2025**, *17*, 3836. [CrossRef]
14. Cheng, X.; Wang, L.; Liu, Y.; Liu, X.Y.; Tan, H.L.; Liu, Y.; Zhang, M.J.; Yan, S. PiLoT: Neural Pixel-to-3D Registration for UAV-based Ego and Target Geo-localization. *arXiv* **2026**, arXiv:2603.20778.
15. Si, X.; Xu, G.; Ke, M.; Zhang, H.; Tong, K.; Qi, F. Relative Localization within a Quadcopter Unmanned Aerial Vehicle Swarm Based on Airborne Monocular Vision. *Drones* **2023**, *7*, 612. [CrossRef]
16. Cai, Y.; Guo, H.; Zhou, K.; Xu, L. Unmanned aerial vehicle cluster operations under the background of intelligentization. In Proceedings of the 2021 3rd International Conference on Artificial Intelligence and Advanced Manufacture (AIAM), Manchester, UK, 23–25 October 2021.
17. Zhang, F.; Shao, X.; Zhang, W. Cooperative fusion localization of a nonstationary target for multiple uavs without gps. *IEEE Syst. J.* **2024**, *18*, 1951–1962. [CrossRef]
18. Garcia, G.; Eskandarian, A. Vision-Based Unmanned Aerial Vehicle Swarm Cooperation and Online Point-Cloud Registration for Global Localization in Global Navigation Satellite System-Intermittent Environments. *Drones* **2026**, *10*, 65. [CrossRef]
19. Xu, H.; Zhao, G.; Bo, Y. UAV–UGV Collaborative Localization in GNSS-Denied Large-Scale Environments: An Anchor-Free VIO–UWB Fusion with Adaptive Weighting and Outlier Suppression. *Drones* **2026**, *10*, 175. [CrossRef]
20. Lee, B.; Sung, S. A study on dual quaternion based cooperative relative navigation of multiple UAVs with monocular vision-inertial integration. *Chin. J. Aeronaut.* **2024**, *37*, 335–354. [CrossRef]
21. Che, F.; Niu, Y.; Li, J.; Wu, L. Cooperative standoff tracking of moving targets using modified Lyapunov vector field guidance. *Appl. Sci.* **2020**, *10*, 3709. [CrossRef]
22. Bai, G.; Liu, J.; Song, Y.; Zuo, Y. Two-UAV intersection localization system based on the airborne optoelectronic platform. *Sensors* **2017**, *17*, 98. [CrossRef] [PubMed]
23. Zhao, J.; Yu, X.; Li, X.; Wang, H. Bearing-only formation tracking control of multi-agent systems with local reference frames and constant-velocity leaders. *IEEE Control Syst. Lett.* **2020**, *5*, 1–6.
24. Zhu, X.; Vanegas, F.; Gonzalez, F.; Sanderson, C. A Multi-UAV System for Exploration and Target Finding in Cluttered and GPS-Denied Environments. In Proceedings of the 2021 International Conference on Unmanned Aircraft Systems (ICUAS), Athens, Greece, 15–18 June 2021.
25. Zhao, L.; Li, R.; Han, J.; Zhang, J. A distributed model predictive control-based method for multidifferent-target search in unknown environments. *IEEE Trans. Evol. Comput.* **2022**, *27*, 111–125.
26. Ibenthal, J.; Meyer, L.; Piet-Lahanier, H.; Kieffer, M. Localization of partially hidden moving targets using a fleet of UAVs via bounded-error estimation. *IEEE Trans. Robot.* **2023**, *39*, 4211–4229. [CrossRef]
27. Peng, J.; Wang, Q.; Jin, B.; Zhang, Y.; Lu, K. Trajectory Optimization to Enhance Observability for Bearing-Only Target Localization and Sensor Bias Calibration. *Biomimetics* **2024**, *9*, 510. [CrossRef] [PubMed]
28. Qian, M.; Chen, W.; Sun, R. A Maneuvering Target Tracking Algorithm Based on Cooperative Localization of Multi-UAVs with Bearing-Only Measurements. *IEEE Trans. Instrum. Meas.* **2024**, *73*, 9516911. [CrossRef]
29. Zhou, K.; Chu, W.; Zhao, P. Monocular Visual Measurement System Uncertainty Analysis and One-Step End-to-End Estimation Upgrade. *Sensors* **2025**, *25*, 7179. [CrossRef] [PubMed]
30. Rahimian, P.; Kearney, J.K. Optimal camera placement for motion capture systems in the presence of dynamic occlusion. In Proceedings of the 21st ACM Symposium on Virtual Reality Software and Technology, Beijing, China, 13–15 November 2015.
31. Du, M.; Zou, H.; Wang, T.; Zhu, K. A Cooperative Target Localization Method Based on UAV Aerial Images. *Aerospace* **2023**, *10*, 943. [CrossRef]
32. Xu, C.; Yin, C.; Huang, D.; Han, W.; Wang, D. 3D target localization based on multi–unmanned aerial vehicle cooperation. *Meas. Control* **2021**, *54*, 895–907.
33. Martens, M.; de Haag, M.U. Cooperative Swarm Geometry Optimization for Assured Navigation with Range Radios in GNSS-Denied Environments. *Eng. Proc.* **2023**, *54*, 38. [CrossRef]

34. Zhu, J.; Song, B.; Zhang, H.; Wang, C. Positioning accuracy and formation analysis of multi-UAV passive positioning system. *J. Phys. Conf. Ser.* **2021**, *1856*, 012055. [CrossRef]
35. Wang, L.; Zhou, S.; Gong, M.; Zhao, P.; Yang, J.; Sui, X. Three-Dimensional Signal Source Localization with Angle-Only Measurements in Passive Sensor Networks. *Remote Sens.* **2024**, *16*, 1319. [CrossRef]

Disclaimer/Publisher's Note: The statements, opinions and data contained in all publications are solely those of the individual author(s) and contributor(s) and not of MDPI and/or the editor(s). MDPI and/or the editor(s) disclaim responsibility for any injury to people or property resulting from any ideas, methods, instructions or products referred to in the content.